EES Batteries

PAPER

View Article Online
View Journal | View Issue

Cite this: *EES Batteries*, 2025, **1**, 1740

Sc/Zn co-doped NASICON electrolyte with high ionic conductivity for stable solid-state sodium batteries

Zichen Li,† Mengdi Zhang,† Yingchun Yan,* Weimin Zhang, Xiuxia Meng and Naitao Yang *

Sodium-ion batteries (SIBs) have emerged as a sustainable alternative to lithium-ion batteries (LIBs), benefiting from the natural abundance and low cost of sodium resources. However, the inherent safety risks of conventional organic liquid electrolytes necessitate the development of robust solid-state electrolytes (SSEs). NASICON-structure $Na_3Zr_2Si_2PO_{12}$ (NZSP) represents a promising SSE candidate due to its superior ionic conductivity, wide electrochemical stability window, and excellent chemical compatibility. Nevertheless, polycrystalline NZSP suffers from high grain boundary resistance and interfacial instability, limiting its practical application. Herein, a Sc^{3+}/Zn^{2+} co-doped strategy was developed to synthesize $Na_{3.2+2x}Zr_{1.8-x}Sc_{0.2}Zn_xSi_2PO_{12}$ (NZSSP-Zn_x, x = 0–0.20), the incorporation of Sc^{3+} stabilizes the highly conductive rhombohedral phase and expands Na^+ transport channels, while Zn^{2+} doping lowers the sintering temperature of monoclinic-to-rhombohedral transition in NZSSP-$Zn_{0.10}$. The synergistic co-doped approach employing NZSSP-$Zn_{0.10}$ demonstrates remarkable enhancement in both bulk and grain boundary conductivity. During thermal processing, the precursor materials undergo *in situ* transformation to generate a Na_3PO_4 secondary phase, exhibiting a high ionic conductivity of 2.41×10^{-3} S cm^{-1}, and a low activation energy of 0.20 eV. The distribution of relaxation times (DRT) method was applied to analyze the time-resolved electrochemical impedance spectroscopy (EIS), elucidating the correlation between dynamic interfacial changes and electrochemical processes at the Na/NZSSP-$Zn_{0.10}$ SSE interface. The Na|NZSSP-$Zn_{0.10}$|Na symmetric cell achieves a high critical current density (CCD) of 0.9 mA cm^{-2} and stable Na plating/stripping for 550 h at 0.1 mA cm^{-2}. The assembled Na|NZSSP-$Zn_{0.10}$|NVP/C demonstrates excellent cycling stability (0.029% decay per cycle over 400 cycles at 0.5 C). This work provides a feasible co-doped approach to optimize NASICON electrolytes for high-performance solid-state sodium batteries.

Received 22nd April 2025,
Accepted 22nd August 2025

DOI: 10.1039/d5eb00075k

rsc.li/EESBatteries

Broader context

Solid-state sodium-ion batteries exhibit enormous potential in addressing the safety issues and performance challenges inherent in traditional liquid batteries, making them a key research direction for next-generation sodium-ion batteries. However, ideal solid-state electrolytes typically need to meet high ionic conductivity at room temperature (>10^{-4} S cm^{-1}) and good interfacial compatibility with solid-state electrode materials. The rhombohedral-phase $Na_3Zr_2Si_2PO_{12}$ (NZSP) exhibits superior Na^+ conductivity, attributed to its lower activation energy (E_a) for ion diffusion resulting from structurally expanded transport channels. In this study, a Sc^{3+}/Zn^{2+} co-doping strategy was developed to synergistically reduce grain boundary resistance, enhance ionic conductivity, and improve interfacial compatibility in the solid electrolyte. The resulting $Na_{3.2+2x}Zr_{1-x}Sc_{0.2}Zn_xSi_2PO_{12}$ (NZSSP-$Zn_{0.10}$)-based solid-state batteries exhibit exceptional cycling stability, positioning this material as a highly promising candidate for next-generation high-performance solid-state batteries.

Introduction

Sodium-ion batteries (SIBs) have emerged as a promising alternative to lithium-ion batteries (LIBs) due to the abundance of sodium reserves, low-cost-effectiveness, and analogous operating principles and cell structures to LIBs.[1–3] However, SIBs employing organic liquid electrolytes face significant safety challenges, including electrolyte leakage and poor thermal stability, which elevate the risks of combustion and explosion. Solid-state electrolytes (SSEs) have been instrumental in overcoming the critical safety challenge of solid-state sodium batteries (SSIBs) by replacing flammable liquid electrolytes.[4–6] The practical adoption of solid polymer electro-

School of Chemical Engineering, Shandong University of Technology, Zibo 255049, China. E-mail: naitaoyang@126.com, yingchyan07@163.com
† These authors contributed equally to this work.

lytes (SPEs) is limited by intrinsic challenges, including low ionic conductivity (<10^{-5} S cm^{-1} at 25 °C) and narrow electrochemical windows (<4 V).[6] Among inorganic solid electrolytes (ISEs), Na-β″-Al_2O_3 demonstrates high ionic conductivity, but extremely high sintering temperature (>1600 °C) limits their large-scale commercialization. Similarly, sulfide-based SSEs despite their superior ionic conductivity, suffer from poor air stability and reactivity with moisture, leading to toxic gas evolution. These intrinsic drawbacks significantly increase fabrication complexity and production costs.[6–8] In contrast, Na Super-Ionic Conductor (NASICON) emerges as the most promising SSE candidate, exhibiting a wide electrochemical stability window (>4 V), excellent interfacial compatibility, low electronic conductivity, and high ionic conductivity (10^{-4}–10^{-3} S cm^{-1}).[5] These properties make NASICON particularly well-suited for large-scale energy storage systems.

NASICON-structured $Na_3Zr_2Si_2PO_{12}$ (NZSP), possesses a structure consisting of corner-sharing ZrO_6 octahedra and PO_4/SiO_4 tetrahedra. This arrangement forms a three-dimensional network, and the interconnected channels within the framework function as efficient Na^+ transport pathways, enhancing the ionic conductivity of the electrolyte.[9] The crystal structure of NZSP is highly tunable based on sintering conditions and composition. NZSP typically crystallizes into a rhombohedral phase at high temperatures ($0 < x < 1.8$, $1.8 < x < 2.3$, space group $R\bar{3}c$) and a monoclinic phase at low temperatures ($1.8 \leq x \leq 2.3$, space group $C2/c$).[10,11] Critically, the rhombohedral phase exhibits superior Na^+ conductivity due to its lower activation energy (E_a) for ion diffusion, derived from the expanded diffusion channels and optimized structural symmetry.[12–14] Using NZSP as a basic structure, researchers have made many attempts to improve grain conductivity by doping metal ions (such as Mg^{2+}, Al^{3+}, Pr^{3+}, Y^{3+}, Lu^{3+}, Ge^{4+}) at the Zr site (r_M = 0.72 Å) of NZSP. By doping with larger metal ions (r_M > 0.72 Å), the Na^+ transport channel can be effectively enlarged, stabilizing the formation of the rhombohedral phase and thereby reducing the activation energy of ion migration.[12,15–19] At the same time, to compensate for the positive charge vacancies generated by the substitution of lower-valence cations, more Na^+ carriers are introduced, thereby increasing the ionic conductivity.[10,19–22] Despite the excellent bulk ionic conductivity (~10^{-3} S cm^{-1}) of NZSP, the high grain boundary resistance and instability at the electrode–electrolyte interface in their polycrystalline structure severely limit practical applications.

Previous studies have demonstrated that incorporating a conductive second phase at the grain boundaries of NZSP effectively reduces grain boundary resistance and promotes the migration of Na^+ at the grain boundaries. The *in situ* self-reconstruction of mesophase components ($Na_2ZrSi_2O_7$ and Na_3PO_4) facilitates the formation of an amorphous NASICON interphase at grain boundaries.[23] This structural evolution significantly enhances intergranular connectivity, resulting in exceptional grain-boundary conductivity reaching 36 mS cm^{-1}. This value represents a sevenfold enhancement compared to the baseline NZSP electrolyte (5.1 mS cm^{-1}). Moreover, La-doped NZSP can form a Na_3PO_4 second phase, which facilitates ion transport along the grain boundaries. However, this approach may also introduce insulating impurity phases, such as $LaPO_4$ and La_2O_3 may be generated during the doping process, which can seriously hinder the transport of Na^+.[24] Therefore, developing a strategy for self-forming conductive second phases without extrinsic dopants is crucial for improving the grain boundary conductivity of NZSP.

In this work, Sc^{3+}/Zn^{2+} co-doped $Na_{3.2+2x}Zr_{1.8-x}Sc_{0.2}Zn_xSi_2PO_{12}$ (NZSSP-Zn_x, x = 0–0.20) were designed by conventional solid-state reaction (Fig. 1a). The incorporation of Sc^{3+} serves to expand Na^+ transport channels while stabilizing the rhombohedral phase, whereas Zn^{2+} doping effectively lowers the sintering temperature of rhombohedral NZSP and enhances electrolyte densification. Sc^{3+}/Zn^{2+} co-doped creates additional Na^+ vacancies, yielding remarkable improvements in ionic conductivity (2.41×10^{-3} S cm^{-1}) and reduced activation energy (0.20 eV). During the sintering process, raw materials *in situ* form a Na_3PO_4 secondary phase, further optimizing the Na^+ transport dynamics at the grain boundaries. This phase significantly improves Na^+ transport dynamics, as revealed by the distribution of relaxation times (DRT) analysis of *in situ* electrochemical impedance spectroscopy (EIS) data. The optimized NZSSP-$Zn_{0.10}$ develops a stable SEI layer during cycling by uniform Na deposition and stripping. When implemented in a Na|NZSSP-$Zn_{0.10}$|NVP/C full cell, this electrolyte demonstrates outstanding rate capability and long cycling stability (only 0.029% capacity decay in each cycle over 400 cycles at 0.5 C).

Results and discussion

The crystal structure of the NZSSP-Zn_x (x = 0–0.20) electrolytes was analyzed using X-ray diffraction (XRD). As shown in Fig. 1b, all observed diffraction peaks aligned precisely with the standard NASICON structure, confirming the integrity and consistency of the material's crystalline framework. Notably, the peaks at 19.2°, 27.5°, and 34.5° are critical for distinguishing between monoclinic and rhombohedral phases.[13] The XRD pattern of NZSP, displayed in Fig. S1a, exhibits a typical monoclinic structure characterized by a lower peak intensity at 19.2° compared to 19.6°, along with distinct double peaks at 27.5° and 34.5°.[10,11] The magnified view of the XRD pattern (Fig. 1b), reveals that as the Zn ion doping level increases, the peak intensity at 19.2° gradually surpasses that at 19.6°. Simultaneously, the double peaks initially at 27.5° and 34.5° tend to merge into a single peak, with peak positions shifting to lower angles. These observations indicate that Zn ion doping effectively promotes the NASICON structure's transformation from the monoclinic to the rhombohedral phase at reduced temperatures, highlighting the critical role of Zn doping in modulating the material's crystalline framework.[17–19] Besides, the Na_3PO_4

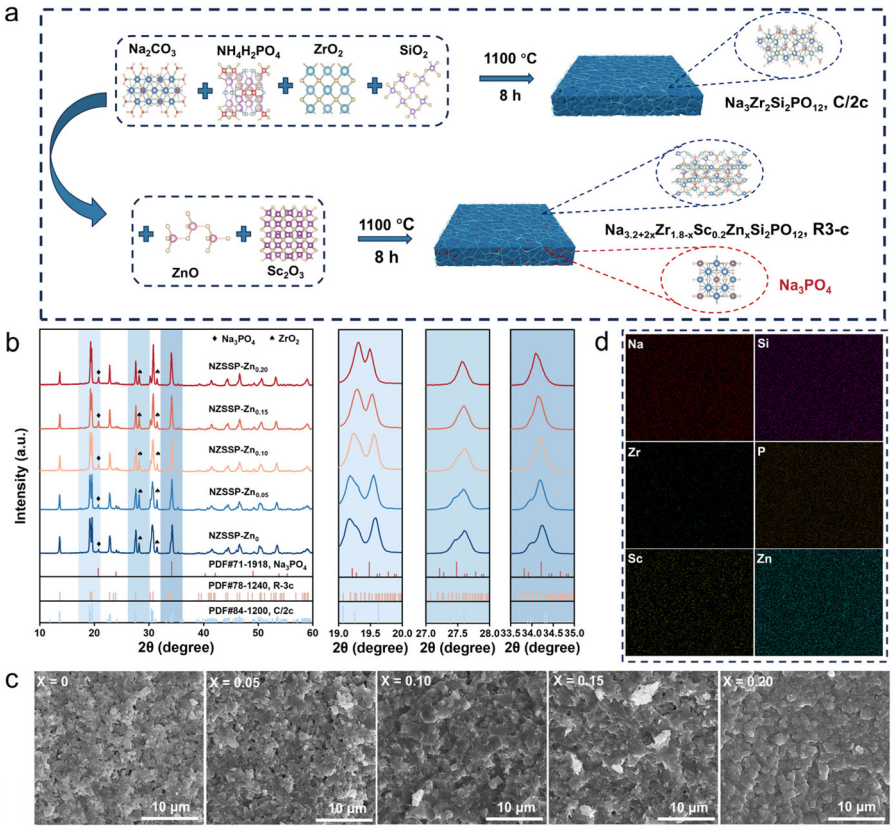

Fig. 1 (a) Schematic diagram of the NASICON-type SSE synthesis process. (b) XRD patterns and magnified partial views. (c) SEM images of NZSSP-Zn_x (x = 0–0.20) surface section. (d) EDS mapping of NZSSP-$Zn_{0.10}$.

secondary phase was identified in the XRD patterns of NZSSP-Zn_x (x = 0–0.20), which arises from excess sodium carbonate and ammonium dihydrogen phosphate at high temperatures. This Na_3PO_4 phase is predominantly distributed along the grain boundaries of the electrolyte, contributing to increased electrolyte density and reduced grain boundary resistance during Na^+ diffusion. Consequently, it effectively facilitates the rapid transport of Na^+ at the grain boundaries. This improved ion mobility at the grain boundaries is crucial for optimizing the functionality of solid-state electrolytes.[5,25–27]

The surface morphology of NZSSP-Zn_x (x = 0–0.20) pellets was analyzed *via* Scanning Electron Microscopy (SEM) for microstructural characterization (Fig. 1c). As shown in Fig. S1b, the surface SEM image of NZSP, reveals that the electrolyte pellets consist of numerous small grains with distinct grain boundaries. Similarly, the SEM image of NZSSP-Zn_0 also shows small grains and clear grain boundaries. Interestingly, with the progressive increase in Zn ion content, the grain size of the electrolyte gradually enlarges, accompanied by a corresponding blurring of the grain boundaries. This structural evolution effectively diminishes the obstacles encountered by Na^+ during transport, thereby significantly enhancing the overall Na^+ mobility and facilitating more efficient ion conduction within the electrolyte.[10,17,28] Notably, when Zn ion doping exceeds a certain level (x > 0.10), the grains of the electrolyte pellets exhibit anisotropic overgrowth, resulting in the formation of crack defects within the grains. This phenomenon disrupts the densification of the electrolyte pellets and impedes Na^+ transport across grain boundaries.[15,29] To confirm the successful incorporation of Sc and Zn ions into the main phase of the electrolyte, elemental distribution in the NZSSP-$Zn_{0.10}$ electrolyte was analyzed *via* energy-dispersive spectroscopy (EDS). The elemental mapping demonstrates a homogeneous distribution of Na, Zr, Si, P, Sc, and Zn (Fig. 1d), confirming the successful integration of Sc^{3+} and Zn^{2+} into the main phase of the electrolyte.

The EIS profiles of NZSSP-Zn_x (x = 0–0.20) electrolyte pellets were measured over a temperature range of 30–100 °C (Fig. 2a, S2a, and S3). The ionic conductivity (σ_t) of the electrolyte pellets exhibits an initial increase followed by a subsequent decrease as the Zn ion content gradually increases. Specifically, the σ_t of NZSSP-Zn_0 is measured to be 9.80×10^{-4} S cm^{-1}, which is significantly higher than that of NZSP (2.13×10^{-4} S cm^{-1}). With the incorporation of Zn ions, the σ_t of NZSSP-$Zn_{0.10}$ reaches 2.41×10^{-3} S cm^{-1}. However, with further increments in Zn ion content, the σ_t of NZSSP-$Zn_{0.15}$ and NZSSP-$Zn_{0.20}$ decreased to 1.25×10^{-3} S cm^{-1} and 1.02×10^{-3} S cm^{-1}, respectively (Table S1 demonstrates detailed date

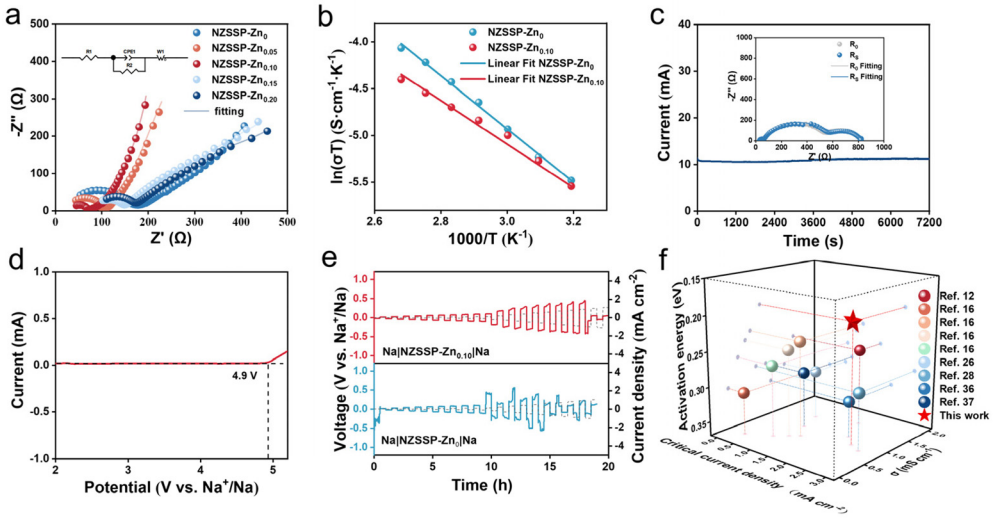

Fig. 2 (a) EIS curves of NZSSP-Zn_x (x = 0–0.20) at room temperature (inset shows the corresponding equivalent circuit model). (b) Arrhenius plots of NZSSP-Zn_0 and NZSSP-$Zn_{0.10}$. (c) Current–time curves of the Na|NZSSP-$Zn_{0.10}$|Na symmetric cell. (d) LSV curves of NZSSP-$Zn_{0.10}$ (inset shows the EIS at initial and steady states). (e) Comparison of critical current density between NZSSP-$Zn_{0.10}$ and NZSSP-Zn_0. (f) A comparison of typical performance with reported Na^+ SSEs.

on ionic conductivity for NZSSP-Zn_x (x = 0–0.20) electrolyte pellets), which attributed to the formation of crack defects within the grains due to grain anisotropic overgrowth, thereby compromises ionic conductivity.[17,30,31] The enhanced ionic conductivity achieved through the doping of $Na_3Zr_2Si_2PO_{12}$ with Sc and Zn ions can be attributed to two primary factors: (1) the slightly larger ionic radius of Sc ions (0.745 Å) and Zn ions (0.74 Å) compared to Zr ions (0.72 Å), stabilize the rhombohedral phase with a larger unit cell volume, thereby creating a more spacious pathway for Na^+ transport; (2) the introduction of Zn ions promotes the densification of NZSSP-$Zn_{0.10}$, while the presence of Na_3PO_4 as a secondary phase at the grain boundaries reduces grain boundary resistance, further minimizing obstacles to Na^+ migration.[13,17]

The activation energy for ion transport was calculated according to the Arrhenius equation (Fig. 2b and S2b), NZSSP-$Zn_{0.10}$ with rhombohedral in NASICON phase exhibits an exceptionally low activation energy of 0.20 eV, significantly lower than those of NZSP (0.31 eV) and NZSSP-Zn_0 (0.24 eV). This reduction in activation energy reflects that NZSSP-$Zn_{0.10}$ creates a more spacious migratory pathway, facilitating the transport of Na^+. Furthermore, the presence of Na_3PO_4 at the grain boundaries reduces the resistance experienced by Na^+ during grain boundary transport, thereby significantly accelerating the Na^+ transport process. Due to this structural optimization, the Na^+ transference number (t_{Na^+}) of NZSSP-$Zn_{0.10}$ is 0.98, higher than that of NZSSP-Zn_0 (0.79), indicating a stronger Na^+ transport capability in NZSSP-$Zn_{0.10}$ (Fig. 2c and S4).[32,33] The electrochemical window of the NZSSP-Zn_x (x = 0–0.20) electrolyte was evaluated by linear sweep voltammetry (LSV) (Fig. 2d). NZSSP-$Zn_{0.10}$ exhibits an optimal electrochemical stability window of 4.9 V, exceeding the stability windows of other NZSSP-Zn_x (x = 0, 0.05, 0.15, 0.20) electrolytes (Fig. S5). The critical current density (CCD) serves as a key indicator for evaluating interfacial stability in Na|NZSSP-Zn_0|Na and Na|NZSSP-$Zn_{0.10}$|Na symmetric cells.[34,35] The Na plating/stripping plots with progressively increasing current densities are shown in Fig. 2e. Compared with NZSSP-Zn_0, which exhibits a CCD of only 0.1 mA cm^{-2}. The irregular voltage fluctuations of Na|NZSSP-Zn_0|Na symmetric cell can be ascribed to the unstable Na plating/stripping and the formation of dead Na.[23] While the CCD of NZSSP-$Zn_{0.10}$ displays a significantly enhanced CCD of 0.9 mA cm^{-2}, demonstrating that its dense structure can suppress the growth of Na dendrites and thereby enhance interfacial stability. The performance metrics achieved in this work belong to a high level among the existing literature reports (Fig. 2f and Table S2).[12,16,26,28,36,37]

Long-term Na plating/stripping cycling tests of Na|SSEs|Na symmetric cells were performed to further assess the interfacial stability between metallic Na and both NZSSP-Zn_0 and NZSSP-$Zn_{0.10}$ electrolytes (Fig. 3a). At a current density of 0.1 mA cm^{-2} and 30 °C, the Na|NZSSP-Zn_0|Na symmetric cell experienced a micro-short circuit after only 70 h, accompanied by high overpotential (125.5 mV) during testing. In contrast, Na|NZSSP-$Zn_{0.10}$|Na shows steady Na insertion/extraction processes for over 650 h with significantly lower overpotential (66.5 mV). As shown in Fig. 3b and S6, the Tafel curves reveal superior interfacial kinetics for NZSSP-$Zn_{0.10}$ with an exchange current density (2.21×10^{-2} mA cm^{-2}), which is higher than that of NZSSP-Zn_0 (0.96×10^{-2} mA cm^{-2}). These results demonstrate that Zn incorporation substantially improves the interfacial contact between the Na metal and the NZSSP-$Zn_{0.10}$ electrolyte, establishing a more kinetically stable charge transfer interface.[38] Furthermore, the interfacial stability of the Na|| Na symmetric cells was systematically investigated through

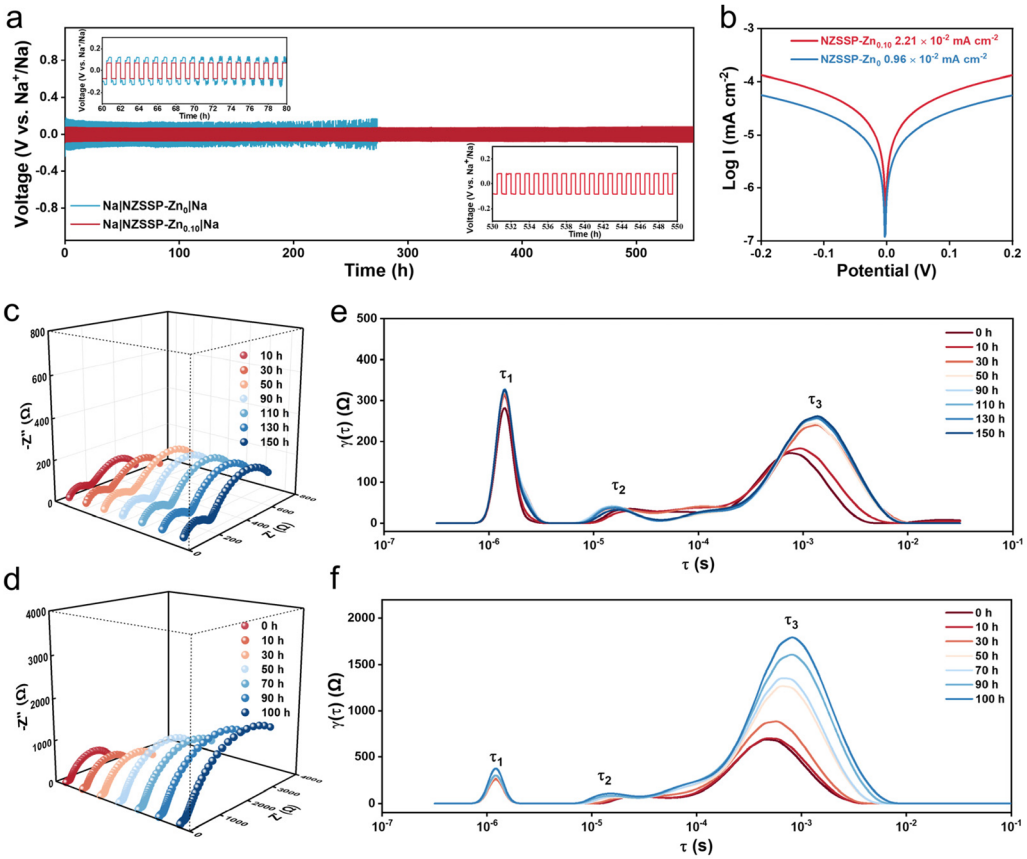

Fig. 3 (a) Cycling performance of Na|SSEs|Na symmetric cells at 0.1 mA cm^{-2}. (b) Tafel plots of NZSSP-$Zn_{0.10}$ and NZSSP-Zn_0 symmetric cells. EIS curves at different cycling times of (c) NZSSP-$Zn_{0.10}$ and (d) NZSSP-Zn_0 symmetric cell. (e) NZSSP-$Zn_{0.10}$ and (f) NZSSP-Zn_0 symmetric cell of EIS curves of different cycle times for distribution relaxation time related function $\gamma(\tau)$.

time-resolved EIS during galvanostatic cycling. Specifically, the Na|NZSSP-$Zn_{0.10}$|Na symmetric cell demonstrated stable operation for 150 h, with time-resolved EIS capturing the temporal evolution of interfacial properties. Parallel testing of the Na|NZSSP-Zn_0|Na symmetric cell was conducted for 100 h under identical experimental conditions to enable direct comparison of interfacial behaviors. As illustrated in Fig. 3c and Table S3, the time-dependent Nyquist plots for the Na|NZSSP-$Zn_{0.10}$|Na symmetric cell reveal distinct electrochemical characteristics. The intercept on the real axis corresponds to the bulk resistance (R_b) of the NZSSP-$Zn_{0.10}$ electrolyte pellet. The first semicircle represents the grain boundary resistance (R_{gb}) of NZSSP-$Zn_{0.10}$, while the second semicircle is attributed to the interfacial resistance (R_{int}) at the Na/NZSSP-$Zn_{0.10}$ interface.[39] The Na|NZSSP-Zn_0|Na symmetric cell exhibited an initial interfacial resistance of 1551 Ω, which increased dramatically to 4596 Ω after 100 h. This interfacial degradation leads to higher overall resistance, corresponding to uneven Na plating and stripping. In contrast, the Na|NZSSP-$Zn_{0.10}$|Na symmetric cell exhibited an initial interfacial resistance of 407.8 Ω and a total resistance of 567.1 Ω. During cycling up to 30 h, R_{int} increases gradually to 567.2 Ω with a corresponding rise in total resistance to 740.98 Ω, attributed to the formation of intermediate phases at the interface. After 50 h, the interfacial resistance stabilizes at 567.3 Ω with a corresponding total resistance of 764.8 Ω. Notably, the interfacial impedance remained relatively constant until 150 h without significant fluctuations (Fig. 3d and Table S4), indicating better Na/NZSSP-$Zn_{0.10}$ interface contact compared to the undoped NZSSP-Zn_0 electrolyte. Such remarkably stable behavior confirms that NZSSP-$Zn_{0.10}$ develops robust interfacial properties during prolonged cycling.

To elucidate the dynamic interfacial changes at the Na/SSE interface and their correlation with interfacial electrochemical processes, the DRT method was employed to analyze the time-resolved EIS. Each relaxation time in the DRT spectrum corresponds to a distinct electrochemical process. The DRT analysis of the Na|SSEs|Na symmetric cells revealed three prominent peaks, denoted as τ_1, τ_2, and τ_3 (Fig. 3e and f). Specifically, the relaxation time τ_1 is associated with the resistive properties of grain boundaries in the SSE, directly reflecting the efficiency of Na^+ transport within the grain boundary regions of the electrolyte. τ_2 is attributed to the solid–electrolyte interphase (SEI) at the Na/SSE interface. Meanwhile, τ_3 corresponds to the charge transfer process of Na^+ at the Na/SSE interface.[18,40,41] In comparison to the Na|NZSSP-Zn_0|Na symmetric cell, the

Na|NZSSP-$Zn_{0.10}$|Na symmetric cell exhibited a lower τ_1 peak intensity, suggesting reduced Na^+ transport resistance across the grain boundaries of the NZSSP-$Zn_{0.10}$ electrolyte. As the cycling progressed, τ_2 shifted slightly toward higher frequencies, which was attributed to the formation of the SEI layer during the initial stages of cycling. Concurrently, the τ_3 peak intensity stabilizes after 50 h, indicating that the Na|NZSSP-$Zn_{0.10}$|Na symmetric cell gradually forms a stable SEI layer during cycling. These findings suggest that the Na|NZSSP-$Zn_{0.10}$|Na symmetric cell develops a stable SEI layer during cycling, which enhances Na^+ transport kinetics, promotes uniform Na deposition and stripping, and effectively suppresses interfacial side reactions.[39,42] In contrast, the Na|NZSSP-Zn_0|Na symmetric cell exhibits a continuous increase in τ_3 peak intensity, indicative of ongoing side reactions at the Na/NZSSP interface. These reactions result in progressive deterioration of interfacial conditions and a sustained increase in resistance.

To investigate the chemical composition of the SEI at the Na/NZSSP-$Zn_{0.10}$ interface during Na plating/stripping processes, X-ray photoelectron spectroscopy (XPS) analysis was employed to analyze the electrolyte surface before and after cycling. A clear increase in the Na 1s peak intensity is observed in the XPS spectra of NZSSP-$Zn_{0.10}$ after cycling, reflecting Na enrichment at the interface. This change directly correlates with the detected alterations in the core-level spectra. As verified in the positions of Zr 3d, Sc 2p, and Zn 2p XPS spectra, the binding energy peaks remain largely invariant, demonstrating the exceptional chemical stability of NZSSP-$Zn_{0.10}$ against the corrosive effects of highly reducing Na metal. Moreover, the Si 2p peak exhibits a shift toward lower binding energy after cycling, indicative of a slight reduction of Si^{4+}.[37] The P 2p spectra consistently exhibited a P peak at approximately 133.1 eV both before and after cycling, stemming from the P–O bonds in NZSSP-$Zn_{0.10}$ and Na_3PO_4.[27,43] Notably, a new peak emerged in the post-cycling P 2p spectra at 129.8 eV, corresponding to the Na_3P peak, and a distinct O 1s peak at 529.7 eV attributed to Na_2O (Fig. 4a and S7).[44,45] The formed SEI layer ensures uniform electric field distribution, suppresses continuous side reactions at the interface, and accelerates Na^+ transport at the interface, thereby achieving stable cycling of the Na/NZSSP-$Zn_{0.10}$ interface. In contrast, after cycling, the Si 2p peak of NZSSP-Zn_0 shifted slightly to lower binding energy, indicating Si^{4+} reduction.[19] Meanwhile, the peaks of Zr 3d, Sc 2p, and P 2p shifted to higher binding energy, suggesting oxidation of NZSSP-Zn_0 during cycling (Fig. 4b and S8). Such an unstable interface is prone to causing non-uniform Na plating/stripping, leading to increased polarization and dendrite formation, which can pose potential risks to battery performance and safety.[24] The

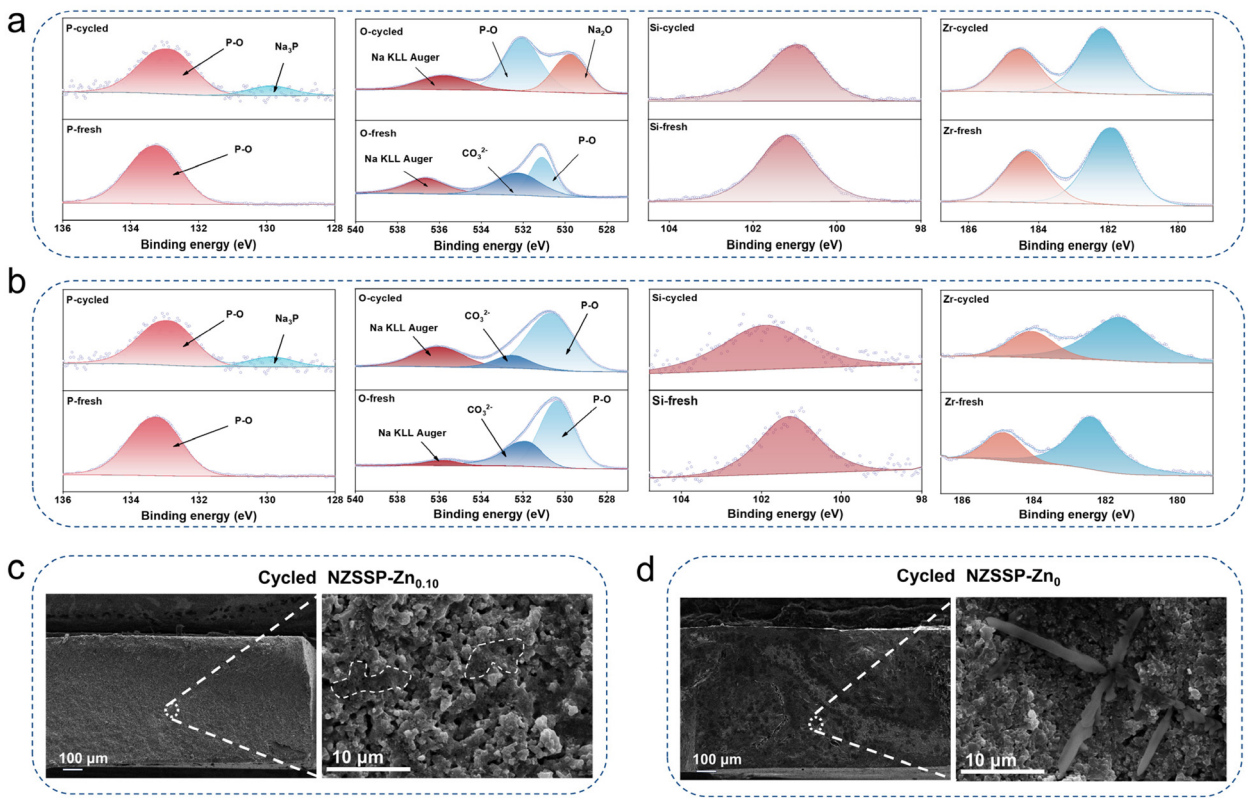

Fig. 4 (a) XPS spectra of P 2p, O 1s, Si 2p, and Zr 3d on the surface of NZSSP-$Zn_{0.10}$ before and after galvanostatic cycling. (b) XPS spectra of P 2p, O 1s, Si 2p, and Zr 3d on the surface of NZSSP-Zn_0 before and after galvanostatic cycling. Cross-sectional and local magnified view SEM images of (c) NZSSP-$Zn_{0.10}$ and (d) NZSSP-Zn_0 sodium symmetric cells after cycling.

surface morphology of the cycled NZSSP-$Zn_{0.10}$ electrolyte was observed by SEM to verify its inhibitory effect on Na dendrite growth (Fig. 4c and d). The NZSSP-Zn_0 electrolyte exhibits severe Na dendrite formation, with dendritic structures propagating through internal pore channels. In contrast, only a small number of vitreous Na dendrites were obtained along the grain surfaces within the NZSSP-$Zn_{0.10}$ electrolyte. This significant difference strongly demonstrates the superiority of the NZSSP-$Zn_{0.10}$ electrolyte in inhibiting Na dendrite growth by regulating uniform Na plating and stripping.[46–49] Furthermore, to directly assess the structural stability of the NZSSP-$Zn_{0.10}$electrolyte, XRD analysis was carried out on the electrolyte after cycling in the Na|NZSSP-$Zn_{0.10}$|Na symmetric cell (Fig. S9). Critically, the XRD patterns reveal that the crystal structure of NZSSP-$Zn_{0.10}$ remains largely unchanged after prolonged cycling, showing no detectable signs of decomposition or phase transformation into less conductive secondary phases. This observation provides direct experimental evidence for the exceptional structural integrity of the Sc/Zn co-doped NASICON electrolyte during electrochemical cycling.

The NZSSP-$Zn_{0.10}$/NZSSP-Zn_0 solid electrolyte was applied in the Na|NASICON SSEs|$Na_3V_2(PO_4)_3$/C (NVP/C) cell to verify the practical application (Fig. 5a). As illustrated in Fig. 5b and c, the Na|NZSSP-$Zn_{0.10}$|NVP/C cell exhibits specific discharge capacities of 111.05, 109.73, 102.81, 96.76, 87.21, 74.32, and 69.77 mAh g^{-1} at current densities of 0.1, 0.2, 0.5, 1, 2 and 4 C (1 C = 117.6 mAh g^{-1}). Even at a high current density of 5 C, the cell still delivers a capacity of 69.77 mAh g^{-1}, higher than that of Na|NZSSP-Zn_0|NVP/C cell (61.13 mAh g^{-1}), respectively. Notably, when the current density was returned to 0.1 C, the

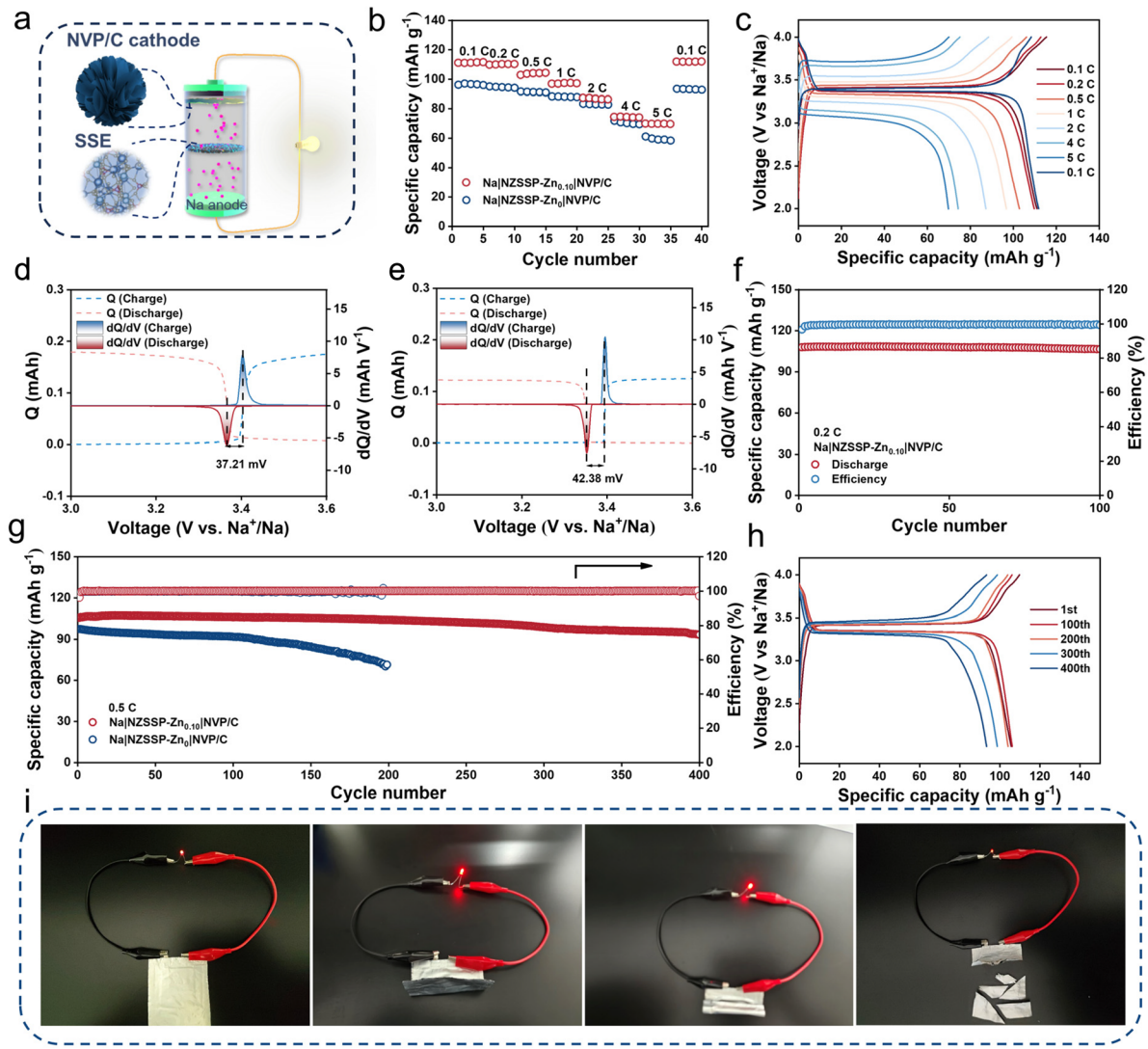

Fig. 5 (a) Schematic diagram of the Na|SSEs|NVP/C cell. (b) Rate performance of the Na|SSEs|NVP/C cell. (c) Charge–discharge curves of the Na|NZSSP-$Zn_{0.10}$|NVP/C cell. Differential capacity profiles of (d) Na|NZSSP-$Zn_{0.10}$|NVP/C and (e) Na|NZSSP-Zn_0|NVP/C. (f) Cycling performance of the Na|NZSSP-$Zn_{0.10}$|NVP/C cell at a current density of 0.2 C. (g) Comparison of cycling performance of the Na|NZSSP-$Zn_{0.10}$|NVP/C and Na|NZSSP-Zn_0|NVP/C cell at a current density of 0.5 C. (h) Charge–discharge curves of the Na|NZSSP-$Zn_{0.10}$|NVP/C cell at a current density of 0.5 C. (i) LED lighted up when Na|NZSSP-$Zn_{0.10}$|NVP/C pouch cell is in different states such as "tiled", "folded", "curled" and "sheared".

discharge capacity recovered to 111.82 mAh g^{-1}, demonstrating exceptional reversibility and stability. The voltage differential capacity (dQ/dV) curve based on 0.1 C was employed to analyze the charging and discharging behavior of the solid-state battery (Fig. 5d and e). The Na|NZSSP-$Zn_{0.10}$|NVP/C cell displayed a charge/discharge plateau at 3.40/3.38 V, corresponding to the reversible redox of V^{3+}/V^{4+} in $Na_3V_2(PO_4)_3$, indicating that the NZSSP-$Zn_{0.10}$ electrolyte facilitates rapid Na^+ reaction kinetics during the Na^+ insertion/extraction process. In contrast, the voltage difference of the charge/discharge plateau corresponding to the dQ/dV curve of the Na|NZSSP-Zn_0|NVP/C cell was 42.38 mV, higher than that of Na|NZSSP-$Zn_{0.10}$|NVP/C cell (37.21 mV). This discrepancy stems from the low Na^+ transport efficiency and inherent kinetic retardation in the NZSSP-Zn_0 electrolyte, collectively limiting ion migration kinetics during redox reactions.

To further evaluate the long-term cycle stability of the Na|SSEs|NVP/C cell, galvanostatic cycling tests were conducted. As shown in Fig. 5f, the Na|NZSSP-$Zn_{0.10}$|NVP/C cell delivered an initial discharge capacity of 108 mAh g^{-1} at 0.2 C, which corresponds to a high initial coulombic efficiency of 97.67%. Impressively, it maintained a reversible capacity of 106.61 mAh g^{-1} after 100 cycles, corresponding to 98.71% capacity retention relative. Even at a higher current density of 0.5 C, the Na|NZSSP-$Zn_{0.10}$|NVP/C cell exhibited a high initial capacity of 105.72 mAh g^{-1} and demonstrated only 0.029% capacity decay per cycle over 400 cycles, accompanied by an average coulombic efficiency exceeding 99.99% (Fig. 5g and h). In contrast, the Na|NZSSP-Zn_0|NVP/C cell exhibited a rapid capacity decay after 200 cycles, reactions at the electrode–electrolyte interface. These irreversible side reactions triggered progressive interfacial degradation, ultimately compromising the structural integrity of the electrolyte and accelerating performance deterioration. To comprehensively evaluate the practical viability of NZSSP-$Zn_{0.10}$ SSE, Na|NZSSP-$Zn_{0.10}$|NVP/C pouch cell with dimensions of 5.5 cm × 5.5 cm was assembled, and its performance was systematically characterized under mechanical stress (Fig. 5i and S10). The pouch cell consistently powered an LED light even when subjected to extreme deformations, including "flat", "folded", "rolled", and "sheared", demonstrating the excellent mechanical reliability and flexibility of the NZSSP-$Zn_{0.10}$ SSE. The corresponding cycling performance was shown in Fig. S11. These results show its vast development potential and promising prospects in the field of flexible electronics.

Conclusions

In summary, a Sc and Zn co-doped NASICON electrolyte was successfully synthesized *via* a solid-state reaction. The incorporation of Sc^{3+} serves to expand Na^+ transport channels and stabilize the rhombohedral phase, while Zn^{2+} doping effectively reduces the sintering temperature of monoclinic-to-rhombohedral transition temperature in NZSSP-$Zn_{0.10}$. The synergistic effect of Sc^{3+}/Zn^{2+} co-doped introduces additional Na^+ vacancies, leading to a significant improvement in ionic conductivity (2.41×10^{-3} S cm^{-1}) and a reduced activation energy (0.20 eV). Meanwhile, the dynamic evolution of interfacial processes at the Na/SSE interface was systematically investigated through EIS coupled with the DRT analysis. Complementary X-ray photoelectron spectroscopy (XPS) characteristic reveals that the formation of a Na_3P/Na_2O-rich SEI layer effectively mitigates electrolyte degradation and suppresses interfacial resistance growth, thereby inhibiting Na dendrite penetration. Consequently, the Na|NZSSP-$Zn_{0.10}$|Na symmetric cell achieves a high CCD of 0.9 mA cm^{-2} and sustains stable Na plating/stripping for 550 h at 0.1 mA cm^{-2}. The assembled Na|NZSSP-$Zn_{0.10}$|NVP/C demonstrates excellent cycling stability with only 0.029% capacity decay per cycle over 400 cycles at 0.5 C. Notably, the corresponding pouch cells maintain stable operation under various mechanical deformations, including folding, rolling, and cutting, powering LED lights without performance degradation. The co-doping strategy lays the foundation for applying NASICON in solid-state batteries by concurrently enhancing ionic transport and interfacial stability.

Experimental

Synthesis of NASICON-based solid-state electrolytes

The solid-state electrolyte $Na_{3.2+2x}Zr_{1.8-x}Sc_{0.2}Zn_xSi_2PO_{12}$ (x = 0–0.20) was synthesized by solid-state reaction method. The raw materials Na_2CO_3 (Aladdin, 99.9%), ZrO_2 (Aladdin, 99.9%), SiO_2 (Aladdin, 99.9%), Sc_2O_3 (Aladdin, 99.9%), ZnO (Aladdin, 99%) and $NH_4H_2PO_4$ (Aladdin, 99%) were mixed according to stoichiometric ratios and 5 M% excess P and Na sources were added to compensate for the volatilization of Na and P during high-temperature sintering. Subsequently, the raw materials were mixed and dispersed in an ethanol medium. The mixture was ball milled at 200 rpm for 12 h to form precursors. The dried precursor was pre-sintered at 900 °C for 12 h. Then, it was ball milled again at the same speed for 12 h and dried to obtain precursor powder. The dried precursor was pre-sintered at 900 °C for 12 h. Then, it was ball milled again at the same rotational speed for 12 h and dried to obtain precursor powder. The precursor powder was pressed into pellets using a 15 mm diameter mould. Finally, the pellets were sintered in an alumina crucible at a sintering temperature of 1100 °C, with a ramp-up rate of 3 °C min^{-1} and a ramp-down rate of 3 °C min^{-1}. The sintered electrolyte pellets were polished with 400 and 1000 grit sandpaper to a thickness of about 1 mm.

Material characterizations

The crystal structure of the material was analyzed by X-ray diffraction (XRD, Bruker D8 advance, Cu Kα = 1.5412 Å) over a scanning range of 10° to 60° at a scanning rate of 10° min^{-1}. The synthesized solid-state electrolyte powder was tested, and the XRD spectral data obtained from the tests were compared with standard PDF cards and analyzed using Jade software. The microscopic morphology and elemental distribution of

the electrolytes were observed by field emission scanning electron microscopy (SEM, Sirion200) equipped with an energy dispersive spectrometer (EDS). The chemical composition and bonding environment of the electrolytes were analyzed by X-ray photoelectron spectroscopy (XPS, Thermo Scientific K-Alpha).

Ionic conductivity

The impedance of the solid electrolytes was measured by electrochemical impedance spectroscopy (EIS) with an amplitude of 5 mV and a frequency range of 1 MHz to 0.1 Hz. Before the tests, silver electrodes were uniformly coated on both sides of the electrolyte pellet to act as blocking electrodes. The ionic conductivities (σ) of the electrolytes were obtained according to the following equation:

$$\sigma = \frac{L}{AR}$$

where σ_t, L, A, and R are the total ionic conductivity (S cm^{-1}), thickness (cm), area (cm^2), and resistance (Ω) of the electrolytes, respectively.

Na-ion activation energy

The ionic conductivity of NASICON-based electrolytes, as typical inorganic solid electrolytes, follows an Arrhenius relationship with temperature. The EIS of the NASICON electrolytes was measured at 40–100 °C, and the Na^+ activation energy of the electrolyte was obtained according to the following equation:

$$\sigma = \frac{A}{T}\exp\left(-\frac{E_a}{RT}\right)$$

where E_a is the activation energy, σ is the ionic conductivity of the measured electrolyte, A is the pre-exponential factor (S cm^{-1} K), and T is the absolute temperature (K).

Na-ion transference number

Na|SSEs|Na symmetric cells were assembled in an argon-filled glove box (H_2O and O_2 < 0.1 ppm). The Na-ion transference number (t_{Na^+}) of the electrolyte was obtained according to the following equation:

$$t_{Na^+} = \frac{I_{ss}(\Delta V - I_0R_0)}{I_0(\Delta V - I_{ss}R_{ss})}$$

where ΔV refers to the applied potential (10 mV), I_0 and I_{SS} refer to the initial and stabilized current values before and after polarization, and R_0 and R_{SS} refer to the impedance values before and after polarization.

Linear sweep voltammetry (LSV)

Ag|SSEs|Na asymmetric cells were assembled in an argon-filled glove box (H_2O and O_2 < 0.1 ppm) using a silver electrode as the working electrode and Na metal as the reference electrode. The electrochemical window of the electrolyte was measured by LSV with a scan rate of 1 mV s^{-1} and a scan voltage range of 0 to 6 V.

Na plating/stripping experiments

Na|SSEs|Na symmetric cells were assembled in an argon-filled glove box (H_2O and O_2 < 0.1 ppm) and tested for critical current density and Na plating/stripping at 30 °C.

Assembly of Na|SSEs|NVP/C cells

The CR2032-type NASICON-based solid-state cells were assembled in an argon-filled glove box (H_2O and O_2 < 0.1 ppm) with $Na_3V_2(PO_4)_3$/C (NVP/C) as the cathode and Na metal as the anode. The NVP/C composite cathode was prepared by mixing NVP, NASICON-based electrolyte powder, Super P, and PVDF at a mass ratio of 6 : 2 : 1 : 1 in *N*-methylpyrrolidone solvent. The slurry was then applied to the aluminum foil and vacuum dried at 100 °C for 12 h. The prepared cathodes were cut into discs with a diameter of 12 mm, and the active substance loading of each cathode was approximately 2 mg cm^{-2}. The solid–solid contact problem resulted in poor interfacial contact, which caused a large interfacial resistance. To improve the interfacial contact, 3 μL of liquid electrolyte (1 M $NaClO_4$ in PC = 100 vol% with 5.0% FEC) was used on both sides of the electrolyte. For pouch cell fabrication, the cathode was cut into a rectangle (3.5 cm × 4 cm in size). A mixture of $Na_{3.4}Zr_{1.7}Sc_{0.2}Zn_{0.1}Si_2PO_{12}$ and polytetrafluoroethylene (PTFE) in an ethanol solvent at a mass ratio of 9 : 1, ultrasonicate in an ultrasonic machine until the mixture is uniform, and then dry in an oven at 60 °C. The dried raw materials are rolled into a film with a thickness of approximately 140 μm, and then cut into pieces of 5.5 cm × 5.5 cm for the assembly of pouch batteries. To improve the interfacial contact, 80 μL of liquid electrolyte (1 M $NaClO_4$ in PC = 100 vol% with 5.0% FEC) was used on both sides of the electrolyte.

Author contributions

Z. Li performed the experiment and wrote the initial draft. Y. Yan, M. Zhang, and W. Zhang provided assistance for the experiment. X. Meng and N. Yang provided the experimental ideas and supervised the research activities. N. Yang and W. Zhang also provided funding support. Y. Yan helped write and review this paper. All the authors discussed the results and contributed to the writing of the paper.

Conflicts of interest

The authors declare no competing interests.

Data availability

The data on the results of this study can be obtained from the corresponding author.

The SI file contains additional materials characterization and electrochemical performance data (including Fig. S1–S11 and Tables S1–S4). See DOI: https://doi.org/10.1039/d5eb00075k.

Acknowledgements

This work is supported by the National Natural Science Foundation of China (21978157, 21776175) and the Natural Science Foundation of Shandong Province (ZR2022QB147, ZR2023MB093).

References

1 A. M. Glushenkov, *Energy Mater.*, 2023, **3**, 300010.
2 J. Deng, W.-B. Luo, S.-L. Chou, H.-K. Liu and S.-X. Dou, *Adv. Energy Mater.*, 2018, **8**, 1701428.
3 J. P. Lowen, T. Insinna, T. V. Beatriceveena, M. P. Stockham, B. Dong, S. J. Day, C. P. Grey, E. Kendrick, P. R. Slater, P. A. Anderson and J. W. Makepeace, *EES Batteries*, 2025, (3), 527–540.
4 R. Thirupathi, V. Kumari, S. Chakrabarty and S. Omar, *Prog. Mater. Sci.*, 2023, **137**, 101128.
5 L. Xiang, X. Li, J. Xiao, L. Zhu and X. Zhan, *Adv. Powder Mater.*, 2024, **3**, 100181.
6 C. Zhao, L. Liu, X. Qi, Y. Lu, F. Wu, J. Zhao, Y. Yu, Y.-S. Hu and L. Chen, *Adv. Energy Mater.*, 2018, **8**, 1703012.
7 Y. Lu, L. Li, Q. Zhang, Z. Niu and J. Chen, *Joule*, 2018, **2**, 1747–1770.
8 F. Li, M. Hou, L. Zhao, D. Zhang, B. Yang and F. Liang, *Energy Storage Mater.*, 2024, **65**, 103181.
9 J. B. Goodenough, H. Y. P. Hong and J. A. Kafalas, *Mater. Res. Bull.*, 1976, **11**, 203–220.
10 A. G. Jolley, D. D. Taylor, N. J. Schreiber, E. D. Wachsman and B. Raveau, *J. Am. Ceram. Soc.*, 2015, **98**, 2902–2907.
11 B. Santhoshkumar, P. L. Rao, K. V. Ramanathan, A. K. Bera, S. M. Yusuf, V. R. Hathwar and B. Pahari, *Solid State Sci.*, 2021, **111**, 106470.
12 Q. Wang, C. Yu, L. Li, X. Liu, X. Zhang, G. Gao, Y. Wang and G. Li, *Energy Storage Mater.*, 2023, **54**, 135–145.
13 Y. Shao, G. Zhong, Y. Lu, L. Liu, C. Zhao, Q. Zhang, Y.-S. Hu, Y. Yang and L. Chen, *Energy Storage Mater.*, 2019, **23**, 514–521.
14 F. Han, A. S. Westover, J. Yue, X. Fan, F. Wang, M. Chi, D. N. Leonard, N. J. Dudney, H. Wang and C. Wang, *Nat. Energy*, 2019, **4**, 187–196.
15 L. Ran, A. Baktash, M. Li, Y. Yin, B. Demir, T. Lin, M. Li, M. Rana, I. Gentle, L. Wang, D. J. Searles and R. Knibbe, *Energy Storage Mater.*, 2021, **40**, 282–291.
16 X. Wang, J. Chen, Z. Mao and D. Wang, *Chem. Eng. J.*, 2022, **427**, 130899.
17 J. Wang, T. He, X. Yang, Z. Cai, Y. Wang, V. Lacivita, H. Kim, B. Ouyang and G. Ceder, *Nat. Commun.*, 2023, **14**, 5210.
18 L. Zhang, Y. Liu, J. Han, C. Yang, X. Zhou, Y. Yuan and Y. You, *ACS Appl. Mater. Interfaces*, 2023, **15**, 44867–44875.
19 Q. Zhang, Q. Zhou, Y. Lu, Y. Shao, Y. Qi, X. Qi, G. Zhong, Y. Yang, L. Chen and Y.-S. Hu, *Engineering*, 2022, **8**, 170–180.
20 A. G. Jolley, G. Cohn, G. T. Hitz and E. D. Wachsman, *Ionics*, 2015, **21**, 3031–3038.
21 Z. Zou, N. Ma, A. Wang, Y. Ran, T. Song, Y. Jiao, J. Liu, H. Zhou, W. Shi, B. He, D. Wang, Y. Li, M. Avdeev and S. Shi, *Adv. Energy Mater.*, 2020, **10**, 2001486.
22 B. Ouyang, J. Wang, T. He, C. J. Bartel, H. Huo, Y. Wang, V. Lacivita, H. Kim and G. Ceder, *Nat. Commun.*, 2021, **12**, 5752.
23 B. Wei, S. Huang, X. Wang, M. Liu, C. Huang, R. Liu and H. Jin, *Energy Environ. Sci.*, 2025, **18**, 831–840.
24 Y. Luo, X. Fang, J. Xiao, Z. Huang, J. Xiong, G. Jiang and S. Yuan, *J. Alloys Compd.*, 2024, **991**, 174529.
25 A. Chakraborty, R. Thirupathi, S. Bhattacharyya, K. Singh and S. Omar, *J. Power Sources*, 2023, **572**, 233092.
26 D. Zuo, L. Yang, Z. Zou, S. Li, Y. Feng, S. J. Harris, S. Shi and J. Wan, *Adv. Energy Mater.*, 2023, **13**, 2301540.
27 L. Xiang, Y. Gao, Y. Ding, X. Li, D. Jiang, C. Wu, X. Zhan and L. Zhu, *Energy Storage Mater.*, 2024, **73**, 103831.
28 P. W. Jaschin, C. R. Tang and E. D. Wachsman, *Energy Environ. Sci.*, 2024, **17**, 727–737.
29 Q. Ma, M. Guin, S. Naqash, C.-L. Tsai, F. Tietz and O. Guillon, *Chem. Mater.*, 2016, **28**, 4821–4828.
30 C. Huang, G. Yang, W. Yu, C. Xue, Y. Zhai, W. Tang, N. Hu, Z. Wen, L. Lu and S. Song, *J. Alloys Compd.*, 2021, **855**, 157501.
31 J. Christensen, P. Albertus, R. S. Sanchez-Carrera, T. Lohmann, B. Kozinsky, R. Liedtke, J. Ahmed and A. Kojic, *J. Electrochem. Soc.*, 2011, **159**, R1–R30.
32 Y. Yan, Z. Liu, T. Wan, W. Li, Z. Qiu, C. Chi, C. Huangfu, G. Wang, B. Qi, Y. Yan, T. Wei and Z. Fan, *Nat. Commun.*, 2023, **14**, 3066.
33 H. Tian, S. Liu, L. Deng, L. Wang and L. Dai, *Energy Storage Mater.*, 2021, **39**, 232–238.
34 T. Fuchs, C. G. Haslam, F. H. Richter, J. Sakamoto and J. Janek, *Adv. Energy Mater.*, 2023, **13**, 2302383.
35 H. Wan, Z. Wang, S. Liu, B. Zhang, X. He, W. Zhang and C. Wang, *Nat. Energy*, 2023, **8**, 473–481.
36 J. Jia, T. Liu, Y. Li, J. Yang, H. He, X. Zhu and X. Yao, *ChemSusChem*, 2024, **17**, e202400481.
37 Z. Sun, Y. Zhao, Q. Ni, Y. Liu, C. Sun, J. Li and H. Jin, *Small*, 2022, **18**, 2200716.
38 Y. Gu, H. Ma, X. Fan, H. Tao, X. Yang and L. Z. Fan, *Adv. Funct. Mater.*, 2024, **35**, 2416077.
39 D. Li, X. Wang, Q. Guo, X. Yu, S. Cen, H. Ma, J. Chen, D. Wang, Z. Mao and C. Dong, *Carbon Energy*, 2022, **5**, e299.
40 Y. Guo, S. Pan, X. Yi, S. Chi, X. Yin, C. Geng, Q. Yin, Q. Zhan, Z. Zhao, F. M. Jin, H. Fang, Y. B. He, F. Kang, S. Wu and Q. H. Yang, *Adv. Mater.*, 2023, **36**, 2308493.
41 Y. Lu, C.-Z. Zhao, J.-Q. Huang and Q. Zhang, *Joule*, 2022, **6**, 1172–1198.
42 R. Miao, C. Wang, D. Li, C. Sun, J. Li and H. Jin, *Small*, 2022, **18**, 2204487.
43 S. Wang, H. Xu, W. Li, A. Dolocan and A. Manthiram, *J. Am. Chem. Soc.*, 2017, **140**, 250–257.
44 X. Chi, Y. Zhang, F. Hao, S. Kmiec, H. Dong, R. Xu, K. Zhao, Q. Ai, T. Terlier, L. Wang, L. Zhao, L. Guo, J. Lou, H. L. Xin, S. W. Martin and Y. Yao, *Nat. Commun.*, 2022, **13**, 2854.

45 M. Ma, H. Cai, C. Xu, R. Huang, S. Wang, H. Pan and Y. S. Hu, *Adv. Funct. Mater.*, 2021, **31**, 2100278.
46 X. Jin, Y. Zhao, Z. Shen, J. Pu, X. Xu, C. Zhong, S. Zhang, J. Li and H. Zhang, *Energy Storage Mater.*, 2020, **31**, 221–229.
47 J. Qian, X. Wu, Y. Cao, X. Ai and H. Yang, *Angew. Chem., Int. Ed.*, 2013, **52**, 4633–4636.
48 T. Zhao, X. Zheng, D. Wang, L. Huang, B. Li, X. Liu, H. Yang, Y. Dai, Y. Huang and W. Luo, *Adv. Funct. Mater.*, 2023, **33**, 2304928.
49 Y. Yan, Z. Liu, W. Li, F. Feng, X. Yang, B. Qi, M. Gong, Z. Li, C. Wang, T. Wei and Z. Fan, *Energy Storage Mater.*, 2025, **74**, 103892.